Peter Zietlow*, Tobias Beirau, Boriana Mihailova, Lee A. Groat, Thomas Chudy, Anna Shelyug, Alexandra Navrotsky, Rodney C. Ewing, Jochen Schlüter, Radek Škoda and Ulrich Bismayer

# Thermal annealing of natural, radiation-damaged pyrochlore

DOI 10.1515/zkri-2016-1965
Received June 1, 2016; accepted July 19, 2016; published online August 30, 2016

**Abstract:** Radiation damage in minerals is caused by the α-decay of incorporated radionuclides, such as U and Th and their decay products. The effect of thermal annealing (400–1000 K) on radiation-damaged pyrochlores has been investigated by Raman scattering, X-ray powder diffraction (XRD), and combined differential scanning calorimetry/thermogravimetry (DSC/TG). The analysis of three natural radiation-damaged pyrochlore samples from Miass/Russia [6.4 wt% Th, $23.1 \cdot 10^{18}$ α-decay events per gram (dpg)], Panda Hill/Tanzania (1.6 wt% Th, $1.6 \cdot 10^{18}$ dpg), and Blue River/Canada (10.5 wt% U, $115.4 \cdot 10^{18}$ dpg), are compared with a crystalline reference pyrochlore from Schelingen (Germany). The type of structural recovery depends on the initial degree of radiation damage (Panda Hill 28 %, Blue River 85 % and Miass 100 % according to XRD), as the recrystallization temperature increases with increasing degree of amorphization. Raman spectra indicate reordering on the local scale during annealing-induced recrystallization. As Raman modes around 800 $cm^{-1}$ are sensitive to radiation damage (M. T. Vandenborre, E. Husson, Comparison of the force field in various pyrochlore families. I. The $A_2B_2O_7$ oxides. *J. Solid State Chem.* **1983**, *50*, 362, S. Moll, G. Sattonnay, L. Thomé, J. Jagielski, C. Decorse, P. Simon, I. Monnet, W. J. Weber, Irradiation damage in $Gd_2Ti_2O_7$ single crystals: Ballistic versus ionization processes. *Phys. Rev.* **2011**, *84*, 64115.), the degree of local order was deduced from the ratio of the integrated intensities of the sum of the Raman bands between 605 and 680 $cm^{-1}$ divided by the sum of the integrated intensities of the bands between 810 and 860 $cm^{-1}$. The most radiation damaged pyrochlore (Miass) shows an abrupt recovery of both, its short- (Raman) and long-range order (X-ray) between 800 and 850 K, while the weakly damaged pyrochlore (Panda Hill) begins to recover at considerably lower temperatures (near 500 K), extending over a temperature range of ca. 300 K, up to 800 K (Raman). The pyrochlore from Blue River shows in its initial state an amorphous X-ray diffraction pattern superimposed by weak Bragg-maxima that indicates the existence of ordered regions in a damaged matrix. In contrast to the other studied pyrochlores, Raman spectra of the Blue River sample show the appearance of local modes above 560 K between 700 and 800 $cm^{-1}$ resulting from its high content of U and Ta impurities. DSC measurements confirmed the observed structural recovery upon annealing. While the annealing-induced ordering of Panda Hill begins at a lower temperature (ca. 500 K) the recovery of the highly-damaged pyrochlore from Miass occurs at 800 K. The Blue-River pyrochlore shows a multi-step recovery which is similarly seen by XRD. Thermogravimetry showed a continuous mass loss on heating for all radiation-damaged pyrochlores (Panda Hill ca. 1 %, Blue River ca. 1.5 %, Miass ca. 2.9 %).

**Keywords:** actinide impurities; metamict; pyrochlore; radiation damage; Raman spectroscopy.

***Corresponding author: Peter Zietlow,** Department of Earth Sciences, University of Hamburg, 20146 Hamburg, Germany, E-mail: peter.zietlow@uni-hamburg.de
**Tobias Beirau:** Department of Earth Sciences, University of Hamburg, 20146 Hamburg, Germany; and Department of Geological Sciences, Stanford University, Stanford, CA 94305-2115, USA
**Boriana Mihailova and Ulrich Bismayer:** Department of Earth Sciences, University of Hamburg, 20146 Hamburg, Germany
**Lee A. Groat and Thomas Chudy:** Department of Earth, Ocean and Atmospheric Sciences, University of British Columbia, Vancouver, BC V6T 1Z4, Canada
**Anna Shelyug and Alexandra Navrotsky:** Peter A. Rock Thermochemistry Laboratory and Nanomaterials in the Environment, Agriculture, and Technology Organized Research Unit, University of California Davis, Davis, CA 95616, USA
**Rodney C. Ewing:** Department of Geological Sciences, Stanford University, Stanford, CA 94305-2115, USA
**Jochen Schlüter:** Centrum für Naturkunde, Mineralogisches Museum, Universität Hamburg, 20146 Hamburg, Germany
**Radek Škoda:** Institute of Geological Sciences, Faculty of Science, Masaryk University, 611 37 Brno, Czech Republic

## Introduction

Metamict minerals that is those that have sustained a degree of radiation-induced structural disorder from the decay of incorporated radionuclides are often annealed in

order to establish their original crystalline structure [1–4]. However, recent studies of radiation damage induced by ion beam damage (e.g. [5–7]) show that materials and minerals may respond by different disordering mechanisms, including decomposition into new phases, cation and anion disordering to derivate crystalline structures and the formation of amorphous domains in the recoil-atom cascade. Thus, the thermal recovery of the crystalline state in pyrochlore will depend on the degree of atomic-scale ordering and the microstructure of the damaged domains within the crystalline matrix. In this study, we investigate the recovery of radiation damage in pyrochlores that have different levels of radiation damage.

The pyrochlore structure ($Fd\bar{3}m$) with the ideal formula ${}^{VIII}A_2{}^{VI}B_2{}^{IV}X_6{}^{IV}Y$ is an anion-deficient derivative of the fluorite structure ($AX_2$) type with ordered cation sites [8–11]. Pyrochlore consists of corner-sharing $BX_6$ octahedra and $A_2Y$ chains with eight-fold-coordinated $A$ cations [11–14] (see Figure 1). The 48f position is occupied by the X-anion, while the Y-site anion is located at the 8b position and anion vacancies with respect to the fluorite structure are at the 8a position [13]. X-site oxygen atoms have a variable x parameter from 0.375 (undistorted A-site cubes) to 0.4375 (undistorted B-site octahedra, shown in Figure 1). Materials with pyrochlore structure display a large variety of properties that have important technical applications, e.g. catalytic abilities, luminescence, piezoelectricity, ferro- and ferrimagnetism, and giant magnetoresistance [15].

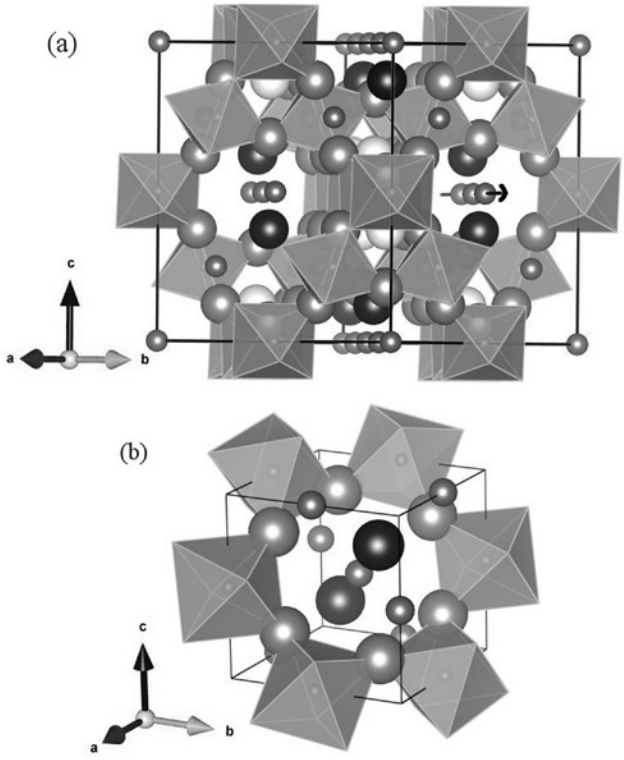


**Fig. 1:** (a) Pyrochlore structure with A-site cations (small dark gray), B-site cations (centers of octahedra), X-site oxygen anions (large gray), Y-site anions (black) and vacancies compared to fluorite structure ('missing' anion in white). The arrow marks channels of A-site cations along [110]. (b) A structural fragment along [111] visualizing a ring of corner-sharing $BX_6$ octahedra.

Natural pyrochlore often occurs with a large variety of incorporated cations. Mainly Na, Ca, U, Th, Y, and REEs occupy the A-site, but also minor elements like $Fe^{2+}$, Mn, $Sn^{2+}$, Sb, Bi, Sr, Ba, Pb, K, and Cs have been found [16]. The B-site can be occupied by Nb, Ta, Ti, $Fe^{3+}$, Zr, and $Sn^{4+}$ [16]. O can occupy the X- as well as the Y-site, whereas OH and F only occupy the latter [16]. The pyrochlore supergroup is divided, based on the B-site cations, into three subgroups, namely pyrochlore with $Nb^{5+}$, betafite with $Ti^{4+}$, and microlite with $Ta^{5+}$ as the major B-site cation [11, 17]. Natural pyrochlores can incorporate up to 30 wt% $UO_2$ and 9 wt% $ThO_2$ [18]. Compositions with pyrochlore structure, hosting actinides, e.g. U, Th, Cm, and Pu, have been successfully synthesized [19–25]. Chakoumakos and Ewing [26] have proposed that actinides with higher valence states like $Np^{6+}$ and $Pu^{6+}$ can be incorporated into an ideal or defect pyrochlore structure at the B-site.

Resulting mainly from the α-decay events of the incorporated actinides, the periodically ordered atomic structure can become disordered, often leading to amorphization (metamictization). This structural damage process has been described in great detail (i.e. [13, 27–30]. The α-decay of the unstable nucleus generates two different types of particles, an α-particle, a ${}^4_2He^{2+}$ core with an energy of ~4.5–5.8 MeV (for actinides), and a heavy recoil nucleus with an energy of ~70–100 keV. The smaller α-particle displaces only several hundreds of atoms, mostly close to the end of its trajectory at ~15–22 μm, inducing Frenkel defects in the structure by elastic collisions. The other particle is a heavier recoil nucleus displacing, in spite of its lower kinetic energy (~86 keV for ${}^{235}U$ recoil from decay of ${}^{239}Pu$), several thousands of atoms in its path of ~30–40 nm through the crystal structure. In zircon ~5000 atoms are displaced per decay event [31, 32]. The difference leading to displaced atoms is attributed to the fact that the α-particle deposits most of its energy by ionization processes; whereas, the recoil nucleus loses its energy by elastic collisions. Therefore, the recoil nucleus introduces atomic recoil- or collision-cascades into the ordered structure. The overlap of these disordered aperiodic regions finally saturates and the long-range order is lost. In pyrochlore, radiation-induced structural changes can be described by the direct impact model [15, 33]. Accordingly, recoil-related discrete regions consisting of

several thousand displaced atoms generate percolation paths by their overlap and create a composite structure of coexisting aperiodic and crystalline regions that are enriched in defects. From the thermodynamical point of view, the radiation-damaged structural state is metastable and can (at least to a certain extent) be recovered by thermal annealing due to activated epitaxial recrystallization or nucleation and crystal growth, depending on the original damage structure. Therefore, the degree of order of metamict natural mineral structures depends on the thermal history with respect to geological processes that can affect, e.g. crystallization and chemical composition.

Using TEM and X-ray diffraction techniques, Lumpkin and Ewing [16] were able to follow the dose related structural damage process in natural pyrochlore. At the earliest stage, isolated α-recoil tracks show little effect. With increasing dose these tracks overlap, producing aperiodic regions (1–5 nm) and a "mottled" diffraction contrast could be observed. This leads to the coexistence of aperiodic and crystalline nanoregions, resulting in a predominant amorphous matrix with embedded crystalline "islands" with further structural damage. Finally, when the lattice fringe periodicity is completely lost and diffraction pattern show diffuse scattering bands, the fully metamict state has been attained. Critical amorphization doses are reported in the order of $10^{18}$–$10^{20}$ α-decay events per gram [16]. Ion irradiation studies on synthetic rare earth titanates have been carried out by Lian et al. [34], who also described several steps of increased disorder prior to amorphization detected by high-resolution transmission electron microscopy (HRTEM). The pyrochlores also showed an increase of their ionic conductivity.

Synthetic and to a smaller extent natural pyrochlores with a broad range of different cation substitutes have been thoroughly investigated [16, 34–41]. Gregg et al. [42] observed additional Raman modes between 700 and 800 $cm^{-1}$ related to U-impurities in the pyrochlore structure.

The annealing-induced recrystallization behavior of moderately to fully metamict, altered natural pyrochlores has been followed among others by differential thermal and thermogravimetric analysis (DTA/TG), revealing strong exothermic reactions and a noticeable weight loss [37, 38, 43].

Because of their long-term stability with respect to radiation-induced damage, pyrochlore-type compounds have been considered as potential hosts for a variety of radionuclides [13, 15, 30]. Therefore, important properties like the critical amorphization dose [18, 36, 44–46] and the leaching behavior [18, 47–53] have been studied in detail. To obtain better understanding of the behavior of pyrochlore under extreme conditions, combined swift heavy-ion irradiation and high-pressure studies have been performed (see [54]). Extensive work has been done on the formation enthalpies of synthetic titanates (e.g. [55, 56]). Nevertheless, knowledge about the thermodynamic stability and physical properties of disordered pyrochlore is still limited [37, 38, 57].

The local structure of synthetic pyrochlore-type materials have been extensively studied by Raman spectroscopy and the observed Raman signals could be assigned to certain phonon modes on the basis of model calculations [6, 7, 10, 45, 48, 49, 52, 58–71].

The motivation of this paper is to address the question of how the initial degree of radiation induced structural damage affects the thermally-induced recrystallization of pyrochlore on different length scales. Therefore, four natural fluorcalciopyrochlores with overall comparable chemistry, but different degrees of structural damage (highly crystalline to fully-metamict) were investigated. In order to better understand the influence of U- and Ta-impurities, one sample with high U/Ta-amount was selected. Local and longer-range probes, such as Raman spectroscopy and powder X-ray diffraction (XRD), respectively, have been used to follow the structural reorganization, while the overall recrystallization behavior has been determined by simultaneous differential scanning calorimetry and thermogravimetric analysis (DSC-TG). The results obtained in this study, reveal a direct dependence between the recrystallization on the short- and long-range and the initial degree of structural damage as well as the occurrence of local modes due to U and Ta contamination.

## Experimental methods

### Electron microprobe analysis

The chemical composition of the pyrochlore was determined by electron microprobe analysis (CAMECA Camebax microbeam SX SEM system), averaging over 9–65 analysis points with an acceleration voltage of 15 keV and a probe current of 20 nA. The beam diameter was set at 1 μm and ZAF correction was used for intensity-mass correlation. Standards used were LiF (F-*K*α), albite (Na-*K*α), andradite (Ca-*K*α, Fe-*K*α), $MnTiO_3$ (Ti-*K*α), $SrTiO_3$ (Sr-*L*α), $ZrSiO_4$ (Zr-*L*α), $Nb_2O_5$ (Nb-*L*α), ree3 (La-*L*α), ree2 (Ce-*L*β), ree4 (Nd-*L*β), $Ta_2O_5$ (Ta-*L*α), Th glass (Th-*M*α) and $UO_2$ (U-*M*β).

### X-ray powder diffraction

Powder XRD patterns were recorded using a Philips XPert powder diffractometer with Bragg Bretano geometry and Cu-*K*α radiation. Multistep annealing of the ground pyrochlores was carried out in a Thermo-Scientific Laboratory Chamber Furnace K114. The temperature was controlled by an AHLBORN THERM 2420 temperature-measuring

device equipped with a NiCr–Ni thermocouple, which ensured a thermal stability of ±2 K. The samples were annealed for 1 h in air in the temperature range of 500–1000 K. Diffraction measurements were performed after a relaxation time of 30 min.

### Spectroscopy

Raman spectra were recorded from the crystallographic plane (111), respectively. The measurements were performed on polished plane-parallel specimens using a Horiba Jobin-Yvon T64000 triple monochromator system operating in the subtractive regime and equipped with a liquid $N_2$-cooled charge-coupled device (CCD) detector and an Olympus BX41 microscope. Spectra were collected in backscattering geometry without analyzer of the scattered light, using the 514.5 nm line of an $Ar^+$-ion laser and a long-working distance objective with magnification 50×. The Raman spectroscopic system was always calibrated to the position of the Si peak at 520.5 $cm^{-1}$ with a precision of ±0.35 $cm^{-1}$. The measured spectra were reduced by the Bose-Einstein occupation factor $\{I_{reduced} = I_{measured}/[n(\omega, T)+1],\ n(\omega, T) = 1/(e^{\hbar\omega/kT}-1)\}$ and fitted by Lorentzian functions using the software package Origin 8.5, to determine the peak positions, full widths at half maximum (FWHM), and integrated intensities. Before annealing and after the last annealing step the samples were checked for photoluminescence with the 488 nm-laser line and for homogeneity at different spots on the polished (111) surfaces. For vibrational mode assignment the parallel polarized measurements were compared to the cross-polarized incident and outgoing beam. As the structurally damaged samples showed varying 810 $cm^{-1}$ intensities before annealing, areas with a low 605–810 $cm^{-1}$ intensity ratio were chosen for analysis. The samples were annealed in a Linkam stage TS1200EV-10/5 with annealing times of 1 h and a heating/cooling ramp of 15 min per temperature step. Raman measurements were performed at room temperature, respectively.

In order to verify whether in general the compositional disorder in pyrochlore violates the phonon selection rules, additional infrared spectra from the crystalline Schelingen reference sample were collected with a Bruker Equinox Fourier Transform Infrared spectrometer. The conventional pellet technique was used for FTIR. The matrix material was KBr (1 mg powdered sample and 200 mg KBr powder).

### Thermal analysis

Simultaneous DSC-TG analyses were performed with a Netsch STA 449 C instrument. The samples were annealed in a Pt pan in air from room temperature up to 1000 K with a heating rate of 10 K/min. A weak weight loss due to volatile species, as has been observed in other radiation-damaged minerals (e.g. [27]) could not be excluded.

## Results and discussion

### Sample description

The samples (Figure 2) were obtained from the Centrum für Naturkunde – Mineralogical Museum Hamburg,

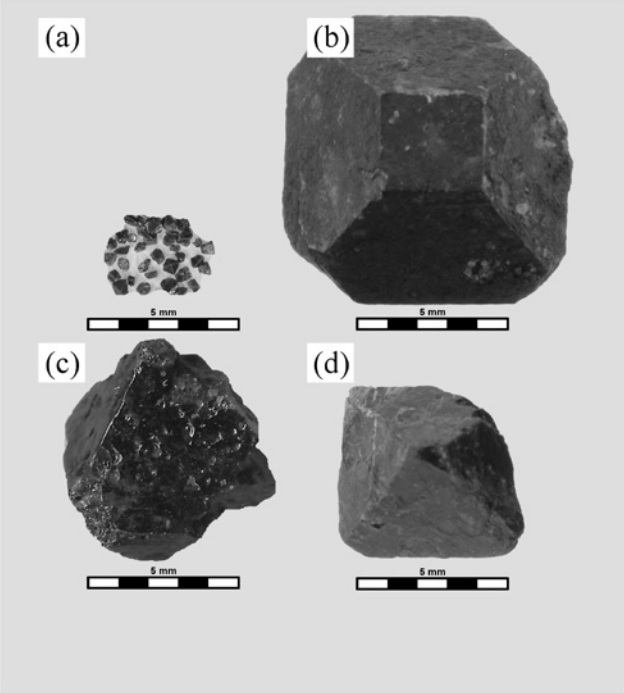


**Fig. 2:** Pyrochlores from (a) Schelingen, Germany, (b) Panda Hill, Tanzania, (c) Blue River, Canada, and (d) Miass, Russia.

(referred as Schelingen and Miass), the Pacific Museum of the Earth of the University British Columbia (referred as Panda Hill) and the collection of Thomas Chudy from the University of British Columbia (referred as Blue River).

All samples were octahedral in form, but the most radiation-damaged samples showed a glassy luster (Figure 2). The Schelingen pyrochlore originates from the Kaiserstuhl carbonatite complex in southwest Germany. With an age of 16 ± 2 Ma [72] it was the youngest sample in this study. Schelingen pyrochlore appeared as brown idiomorphic octahedrons of millimeter size. Panda Hill pyrochlore samples were from the Mbeya mountain range in southwest Tanzania. The corresponding carbonatite complex has been dated to an age of 116 ± 6 Ma [73]. The Panda Hill pyrochlores were brown in color with an idiomorphic octahedral form of 1–3 cm diameter. The initially already partially recrystallized Blue River pyrochlore sample originated from the Upper Fir carbonatite complex in the Monashee Mountains, Canada, whose deposit age is 328 ± 30 Ma (U-Pb dating of zircon) according to the carbonatite data base [74]. The black Blue River sample showed glassy reflection on preserved octahedral surfaces. In addition, black Miass pyrochlores from the Ilmen Mountains in the southern Urals, Russia, showed a glassy luster of their idiomorphic octahedral shape. Ages were reported as 432 ± 12 Ma [75]. Schelingen pyrochlore was selected as a crystalline reference, the Panda Hill sample

as a weakly radiation-damaged, the Blue River pyrochlore as a heavily damaged, containing some ordered crystalline areas, and Miass pyrochlore as a fully-amorphous sample.

The pyrochlore samples had Nb contents ranging from 32.5 to 42.8 wt% at the B-cation site with some content of Ti (0.6–6.0 wt%) or Ta (0.1–14.9 wt%). Ca (7.4–13.1 wt%) and Na (1.6–4.3 wt%) are assigned as A-cations. At the 8a Wyckoff positions there are O and F. All probed pyrochlores have a rather high F content of 2–4 wt%. Incorporated $OH^-/H_2O$ is considered as the main contribution to fractions missing to 100 %.

The results of the electron microprobe analyses are listed in Table 1. The atoms per formula unit were calculated with respect to two B site cations and with the assumption that each element has only one oxidation state. We also assumed that the B site is occupied by two cations and that charge is balanced by molecular $OH^-$, the approximated formulas of the analyzed pyrochlores are:

Schelingen:
$(Na_{0.3}Ca_{1.4}Fe_{0.1}REE_{0.2})(Ti_{0.1}Zr_{0.1}Nb_{1.9})O_6\ (O_{0.8}(OH)_{0.1}F_{0.4})$,
Panda Hill:
$(Na_{0.6}Ca_{1.2}\square_{0.2})(Ti_{0.2}Nb_{1.7})O_6\ (O_{0.1}F_{0.8}\square_{0.1})$,
Blue River:
$(Na_{0.6}Ca_{0.8}U_{0.2}\square_{0.4})\ (Ti_{0.2}Nb_{1.5}Ta_{0.3})O_6(O_{0.2}F_{0.5}\square_{0.3})$,
Miass:
$(Na_{0.7}Ca_{1.0}REE_{0.2}Th_{0.1})(Ti_{0.5}Nb_{1.5})O_6(O_{0.1}F_{0.9})$.

For detailed composition see Table 1.

The only sample containing larger amount of U and Ta is from Blue River, while the other pyrochlore samples rather contain Th- and Ti-impurities. From the actinide content measured by EMP (Table 1) and geologic age the total radiation dose can be calculated using α-decays of the $^{232}$Th-, $^{235}$U- and $^{238}$U-decay series as given by Holland and Gottfried [76]

$$\begin{aligned} D_\alpha = {} & 8\frac{c_U N_A\, 0.9928}{M_{238}\, 10^6}(e^{\lambda_{238}t}-1) \\ & + 7\frac{c_U N_A\, 0.0072}{M_{235}\, 10^6}(e^{\lambda_{235}t}-1) \\ & + 6\frac{c_{Th} N_A}{M_{232}\, 10^6}(e^{\lambda_{232}t}-1) \end{aligned} \quad (1)$$

with U and Th concentrations $c_U$ and $c_{Th}$ in ppm, Avogadro's number $N_A$, molecular weights of parent isotopes $M_{238}$, $M_{235}$ and $M_{232}$, decay constants $\lambda_{238}$, $\lambda_{235}$ and $\lambda_{232}$ [77] and the reported geologic age t in years (Table 2). Actinide contents range from qualitative detection limit to 10.6 wt%, resulting in doses of $<0.1–115.4 \cdot 10^{18}$ decay events per gram by considering the reported crystallization ages of the carbonatite host rocks. After radiation damage, geological conditions may have altered the partially amorphous to an amorphous state of the samples. More recent deformation ages of host rocks were the greenschist-facies metamorphism of the Rocky Mountains and the Urals [75], where temperatures needed for structural healing could have been reached and the crystal structure might have

**Tab. 1:** Chemical composition of pyrochlore samples in wt% oxides.

| | **Schelingen** | | **Panda Hill** | |
|---|---|---|---|---|
| | **(*n* = 25)** | **σ** | **(*n* = 44)** | **σ** |
| $TiO_2$ | 1.1 | 0.2 | 5.1 | 0.3 |
| $ZrO_2$ | 2.0 | 0.4 | 1.0 | 0.4 |
| $Nb_2O_5$ | 60.1 | 1.3 | 61.5 | 1.2 |
| $Ta_2O_5$ | <det.lim. | | 0.7 | 0.3 |
| $Na_2O$ | 2.3 | 0.2 | 5.3 | 0.7 |
| MgO | 0.5 | 0.1 | <det.lim. | |
| CaO | 18.6 | 0.4 | 17.5 | 1.7 |
| FeO | 1.3 | 0.1 | 0.2 | 0.1 |
| SrO | 0.2 | 0.1 | 0.5 | 1.0 |
| $La_2O_3$ | 0.9 | 0.1 | <det.lim. | |
| $Ce_2O_3$ | 5.8 | 0.5 | 0.9 | 0.1 |
| $Nd_2O_3$ | 0.8 | 0.1 | 0.2 | 0.1 |
| $ThO_2$ | <det.lim. | | 1.8 | 0.4 |
| $UO_2$ | <det.lim. | | <det.lim. | |
| $F^-$ | 1.8 | 0.2 | 3.9 | 0.5 |
| Sum | 95.9 | 1.5 | 98.9 | 1.6 |
| −O of F | −0.8 | | −1.6 | |
| Total | 95.1 | | 97.3 | |
| | **Blue River** | | **Miass** | |
| | **(*n* = 64)** | **σ** | **(*n* = 9)** | **σ** |
| $TiO_2$ | 2.9 | 0.1 | 10.0 | 0.3 |
| $ZrO_2$ | <det.lim. | | <det.lim. | |
| $Nb_2O_5$ | 46.5 | 0.8 | 50.6 | 0.5 |
| $Ta_2O_5$ | 18.3 | 0.4 | 2.0 | 0.4 |
| $Na_2O$ | 4.5 | 1.2 | 5.8 | 0.2 |
| MgO | <det.lim. | | <det.lim. | |
| CaO | 10.4 | 0.3 | 14.5 | 0.3 |
| MnO | – | | 0.3 | 0.1 |
| $Fe_2O_3$ | 0.2 | 0.1 | 0.2 | 0.1 |
| SrO | 0.6 | 0.4 | – | |
| $Y_2O_3$ | – | | 0.3 | 0.1 |
| $La_2O_3$ | <det.lim. | | 1.2 | 0.1 |
| $CeO_2$ | <det.lim. | | 3.4 | 0.2 |
| $Pr_2O_3$ | – | | 0.3 | 0.1 |
| $Nd_2O_3$ | <det.lim. | | 1.0 | 0.1 |
| $ThO_2$ | <det.lim. | | 7.2 | 0.6 |
| $UO_2$ | 11.9 | 0.4 | <det.lim. | |
| F | 2.3 | 0.3 | 4.2 | 0.1 |
| Sum | 98.0 | 1.1 | 102.0 | 0.6 |
| −O of F | −1.0 | | −1.8 | |
| Total | 97.0 | | 100.2 | |

Total oxide equivalent corrected for overestimated oxygen ($m_0/m_F$)/2.
'<det.lim.', below quantitative detection limit; '–', not observed.

**Tab. 2:** Ages and doses of pyrochlore samples.

| Sample | Th (wt%) | U (wt%) | Geologic age (Ma) | Dose ($10^{18}$ α-decay $g^{-1}$) |
|---|---|---|---|---|
| Schelingen | <det.lim. | <det.lim. | 16 ± 2[a] | <0.1 |
| Panda Hill | 1.6 ± 0.1 | <det.lim. | 116 ± 6[b] | 1.6 ± 0.1 |
| Blue River | <det.lim. | 10.5±0.1 | 328 ± 30[c] | 115.4 ± 1.0 |
| Miass | 6.4 ±0.1 | <det.lim. | 432 ± 12[d] | 23.1 ± 0.6 |

[a]Lippolt [72], [b]Bell and Blenkinsop [73], [c]Berger et al. [74], [d]Krasnobaev et al. [75].

been (partially) reset. Doses shown in Table 2 are the maximum life-time doses. Microprobe analyses results averaged over 9–65 points and showed only minor chemical deviation, except the Panda Hill sample with narrow chemical zoning towards the sample rim.

## Long-range order: effect of radiation damage and subsequent thermal annealing

The X-ray powder diffraction patterns of the three investigated virgin, radiation damaged pyrochlores show three broad amorphous background features centered at 28.9°, 50.0° and 58.4° 2θ (Panda Hill), 30.3°, 51.5° and 61.4° 2θ (Blue River), and 30.3°, 50.9° and 59.4° 2θ (Miass) (Figure 3). As these features decrease in intensity with increasing annealing temperature, resulting from structural reorganization, the evolution of the amorphous fraction ($X_{amorph}$) could be determined by

$$X_{amorph} = \frac{I_{amorph}}{I_{amorph} + I_{Bragg}} \quad (2)$$

where $I_{amorph}$ and $I_{Bragg}$ are the integrated intensities of the amorphous background and the Bragg signals, respectively (errors are in the order of 5 %) (Figure 4a). The natural crystalline sample from Schelingen served as reference with 9 % disorder probably due to impurities, remaining constant on annealing (Figure 4a). The resulting amorphous fractions of the untreated samples are 28 % (Panda Hill), 85 % (Blue River) and 100 % (Miass). Annealing at T = 1000 K reduced the amorphous fractions to 14 % (Panda Hill), 8 % (Blue River) and 23 % (Miass) with an experimental error of ±2 %.

The diffraction signals of all three radiation damaged samples sharpen and the amorphous background decreases significantly during the step-wise thermal annealing, indicating recrystallization on the mesoscopic length scale. Evolution of the full width at half maximum (FWHM) of the prominent (440) diffraction signal is shown as a function of temperature in Figure 4b. In weakly damaged Panda Hill pyrochlore it gradually decreases from 0.2° to 0.1° 2θ accompanied by a decreasing amorphous fraction from ~24 % to 10 % between 500 and 700 K.

The FWHM of the strongly radiation-damaged Blue River sample is stepwise reduced from 0.3° to 0.1° 2θ between ~650 and 1000 K. The amorphous fraction starts to decrease from ~80 % to <10 % between ~500 and 800 K, but shows a strong reduction at 650 K.

Metamict Miass pyrochlore remains fully-amorphous on the XRD length scale until 790 K. Up to this temperature the diffraction patterns only show a broad Gaussian-shaped amorphous background centered near 30.3° 2θ. The FWHM of this background feature decreases, following a linear trend, during step-wise annealing from room temperature up to 790 K. The recrystallization occurs relatively abrupt between ca. 790 and 850 K, indicated by a sharpening of the diffraction signals and a decrease of the amorphous background. Only a small and constant amorphous fraction (~25 %) remains visible at temperatures above ca. 850 K.

In addition to the broad background signal, the weakly damaged Panda Hill and strongly damaged Blue River pyrochlores show narrow Bragg diffraction signals, which may indicate the presence of small crystalline clusters in the virgin samples. The intensities of these Bragg signals increase on heating between 500 and 700 K and remain constant above 730 K. In the Miass pyrochlore a $NaNbO_3$ phase starts to occur around 820 K. With further annealing up to 1000 K this fraction increases, but remains minor compared to the pyrochlore phase. The Panda Hill and Blue River samples do not show evidences for secondary phases up to annealing temperatures of 1000 K, except a single unidentified diffraction signal at 26.7° in the Panda Hill sample. In all three samples a small amorphous fraction remains visible up to 1000 K. The obtained results show a positive correlation between the degree of structural damage on the long-range scale and the recrystallization behavior, according to the annealing induced sharpening of the diffraction signals.

## Short-range order: effect of radiation damage and subsequent thermal annealing

First-order infrared absorption and Raman scattering spectra of pure pyrochlore can be described by the corresponding optically active irreducible representations at the center of the Brillouin zone [78]. According to group theory, pyrochlore has six Raman and seven infrared active, 12 inactive optical and one acoustic mode [78].

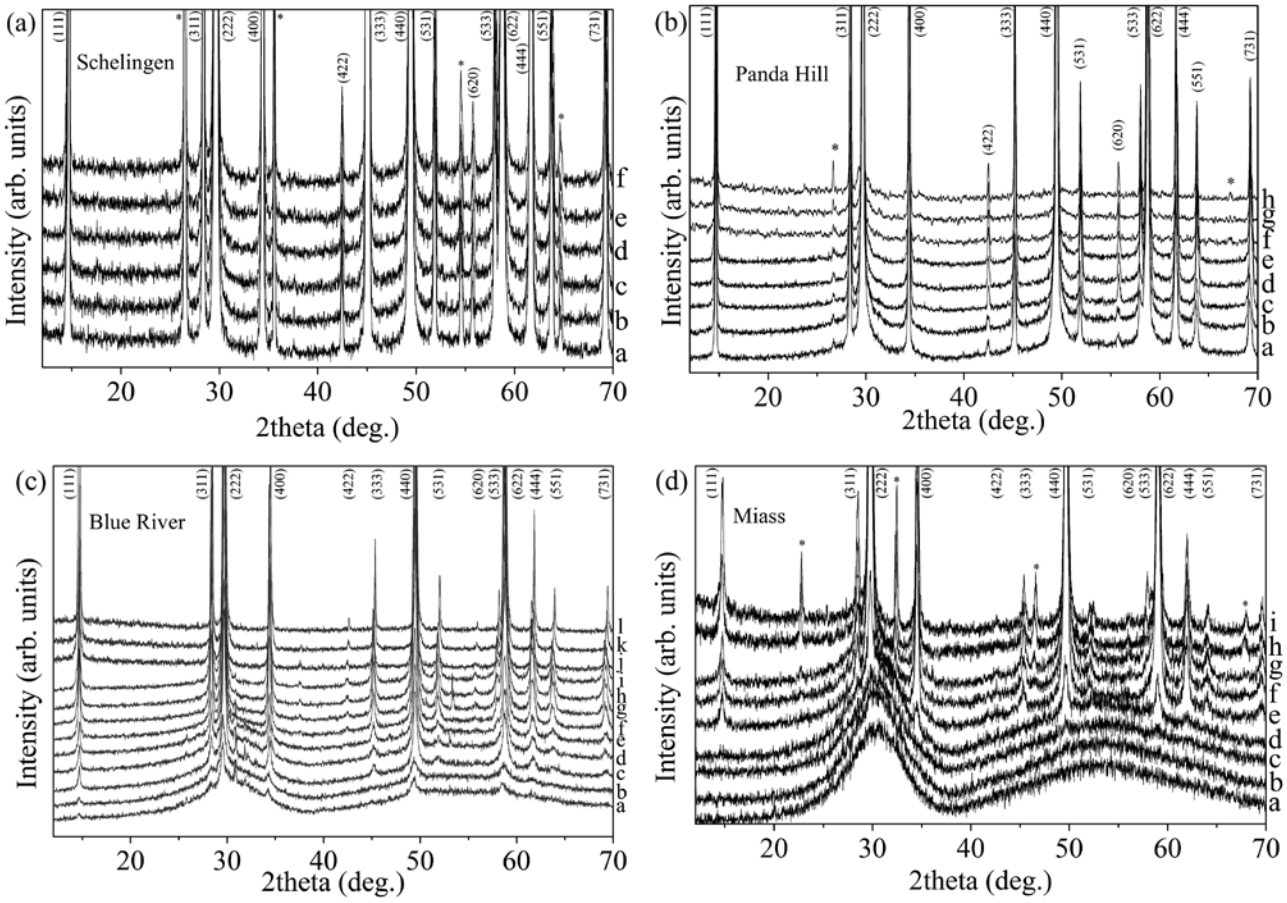


**Fig. 3:** Diffractograms of samples (a) Schelingen (a: 295 K, b: 500 K, c: 700 K, d: 750 K, e: 770 K, f: 780 K), (b) Panda Hill (a: 295 K, b: 500 K, c: 700 K, d: 710 K, e: 720 K, f: 800 K, g: 900 K, h: 1000 K), (c) Blue River (a: 295 K, b: 500 K, c: 550 K, d: 600 K, e: 650 K, f: 700 K, g: 710 K, h: 720 K, i: 730 K, j: 800 K, k: 900 K, l: 1000 K) and (d) Miass (a: 295 K, b: 780 K, c: 790 K, d: 800 K, e: 810 K, f: 820 K, g: 830 K, h: 900 K, i: 1000 K); annealing for 1 h in air. '*' indicates impurities.

The Γ-point phonon modes associated with the occupied Wyckoff positions in pyrochlore are given in Table 3.

The experimentally observed Raman signals are strongly broadened and show considerable overlap. In addition, the metamict Miass pyrochlore shows photoluminescence in the whole measured spectral range. Observed modes are centered at 65, 105, 140, 180, 275 ($T_{2g}$), 365 ($E_g$), 430, 495 ($A_g$), 540 ($T_{2g}$), 605 ($T_{2g}$), 680, 810 and 860 $cm^{-1}$. The Raman band intensities between 450 and 1000 $cm^{-1}$ show in cross-polarized arrangements considerably lower intensities than with parallel-polarization, indicating symmetrical stretching A-modes.

Various studies assigned the fundamental vibrational modes in the range between 140 and 650 $cm^{-1}$ to different chemical compositions as shown for comparison in Figure 5 (after [5–7, 10, 42, 45, 48, 49, 52, 54, 57–67, 71, 79–86]). The observed broad mode above 700 $cm^{-1}$ was assigned either to the $T_{2g}$ vibration [64], to a forbidden mode or a combination of excitations [10, 58]. Frost et al. [87] attributed the complexity of the excitation pattern in the region 600–700 $cm^{-1}$ to Ti–O stretching vibrations combined with peaks due to Nb–O and Y–O stretching bands.

Structural recrystallization on the local length scale can be followed from the evolution of the intensity relation of the sum of the bands in the range 605–680 $cm^{-1}$ and 810–860 $cm^{-1}$ at different annealing steps. This ratio corresponds inversely to the FWHM of the diffraction signals.

The Schelingen pyrochlore with the highest degree of crystallinity among the studied pyrochlore samples shows five main Raman bands at 180, 275, 540, 605 and 810 $cm^{-1}$ (Figures 6–8). The signals are strongly broadened due to structural vacancies and chemical heterogeneity. The latter was observed by microprobe analysis, confirming the presence of several different cations occupying the two structural cation positions.

Weakly damaged Panda Hill pyrochlore shows a band-pattern in the virgin sample which approaches the pattern of the Schelingen sample on annealing.

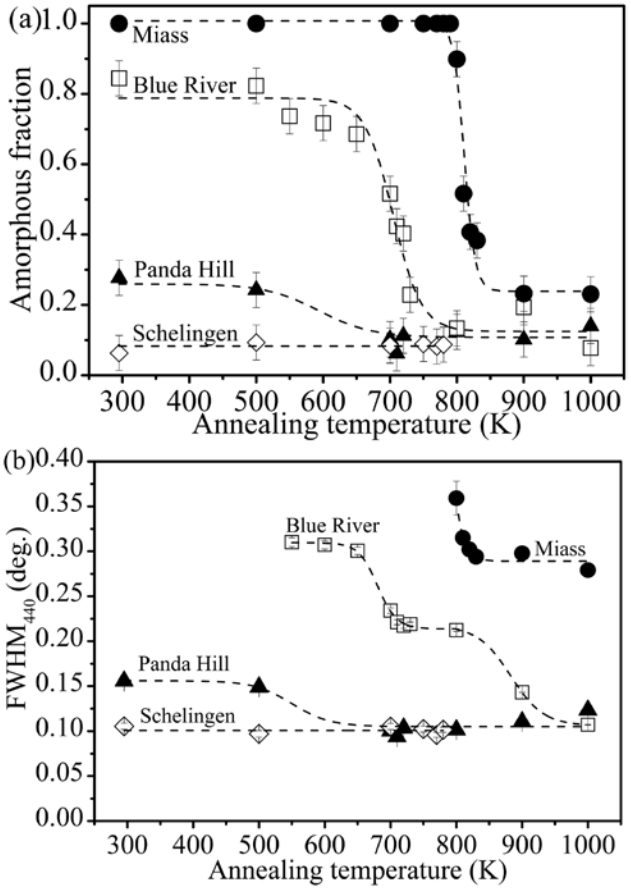


**Fig. 4:** (a) Amorphous fraction deduced from the XRD amorphous background and the total integrated intensities according to $I_{amorph}/(I_{amorph}+I_{Bragg})$ and (b) FWHM of individual (440) powder XRD signals for pyrochlores from Schelingen (◇, $<0.1\cdot10^{18}$ dpa), Panda Hill (▲, $1.6\cdot10^{18}$ dpa), Blue River (□, $115.4\cdot10^{18}$ dpa) and Miass (●, $23.2\cdot10^{18}$ dpa), respectively. The Miass pyrochlore shows no (440) signal exceeding the background noise below 800 K. Lines are guides for eye.

**Tab. 3:** Vibrational modes of the pyrochlore structure ($Fd\bar{3}m$).

| Wyckoff position | Mode (R: Raman-active, IR: IR-active, ina: inactive)[a] |
|---|---|
| A(16d) | $A_{2u}(ina)+E_u(ina)+T_{2u}(ina)+2T_{1u}(IR)$ |
| B(16c) | $A_{2u}(ina)+E_u(ina)+T_{2u}(ina)+2T_{1u}(IR)$ |
| X(48f) | $A_{1g}(R)+A_{2u}(ina)+E_u(ina)+E_g(R)+2T_{2u}(ina)+3T_{2g}(R)+3T_{1u}(IR)+2T_{1g}(ina)$ |
| Y(8b) | $T_{2g}(R)+T_{1u}(IR)$ |

[a]One $T_{1u}$ mode is acoustic, most probably that one related to the lowest-energy cation vibration.

The 810 cm$^{-1}$ signal clearly decreases with annealing temperature but does not disappear completely until 1000 K.

In contrast to all the other studied samples the radiation-damaged Blue River pyrochlore shows four

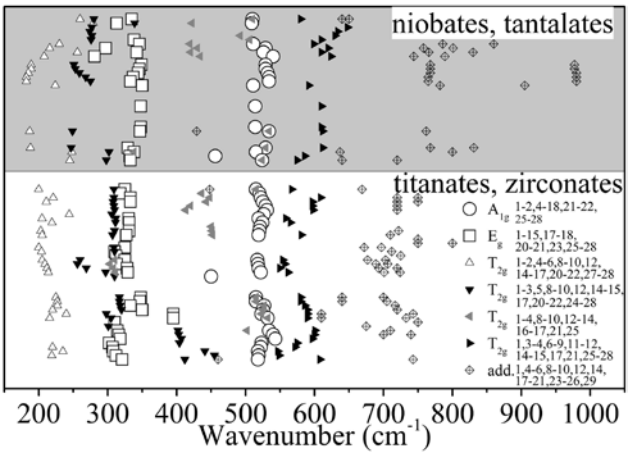


**Fig. 5:** Experimentally observed peak positions of the Raman bands of pyrochlores and their mode assignments [58][1]; [64][2]; [61][3]; [66][4]; [62][5]; [57][6]; [67][7]; [63][8]; [60][9]; [52][10]; [59][11]; [71][12]; [79][13]; [10][14]; [80][15]; [81][16]; [82][17]; [7][18]; [45][19]; [6][20]; [65][21]; [48, 49][22]; [54, 83][23]; [84][24]; [5][25]; [42][26]; [85][27]; [86][28].

additional sharp signals between 700 and 800 cm$^{-1}$ occurring after annealing at temperatures >560 K, although the material appears to be disordered on the long-range length-scale (Figure 3c). The main differences to the other studied pyrochlores are a larger Ta and U content. Sharp modes between 700 and 800 cm$^{-1}$ were assigned to U–O [42] and Nb/Ta-O stretching [88]. Local modes can occur in systems with a large amount of interacting impurities [89] which do not form proper phases. This is in excellent agreement with the observed Raman signals in the same wavenumber region in the Blue River sample (Figure 6b). In order to evaluate the general intensity evolution on annealing these additional sharp signals have been excluded from the calculated intensity ratio (Figure 7). The high U/Ta-impurity concentrations (Table 1) are assumed to dilute the Ca and Nb position, respectively. In this respect, the Blue River pyrochlore is an excellent example to study local mode behavior in natural pyrochlore.

While $Ta^{5+}$ cations have a similar ionic radius to $Nb^{5+}$, their masses (180.9 amu and 92.9 amu, respectively [77]) differ considerably. Despite differences in the compositions of the partially amorphous samples all signal positions could be clearly determined at higher annealing temperatures, also the spectra indicated a generally low influence of the chemistry on the Raman shift (e.g. substitution of Nb by Ta and of A-site cations by U in the Blue River sample).

In the metamict Miass sample, the Raman signal at 810 cm$^{-1}$ is the only one exceeding the photoluminescence. The collected Raman spectra consist of strongly broadened overlapping bands. The photoluminescence

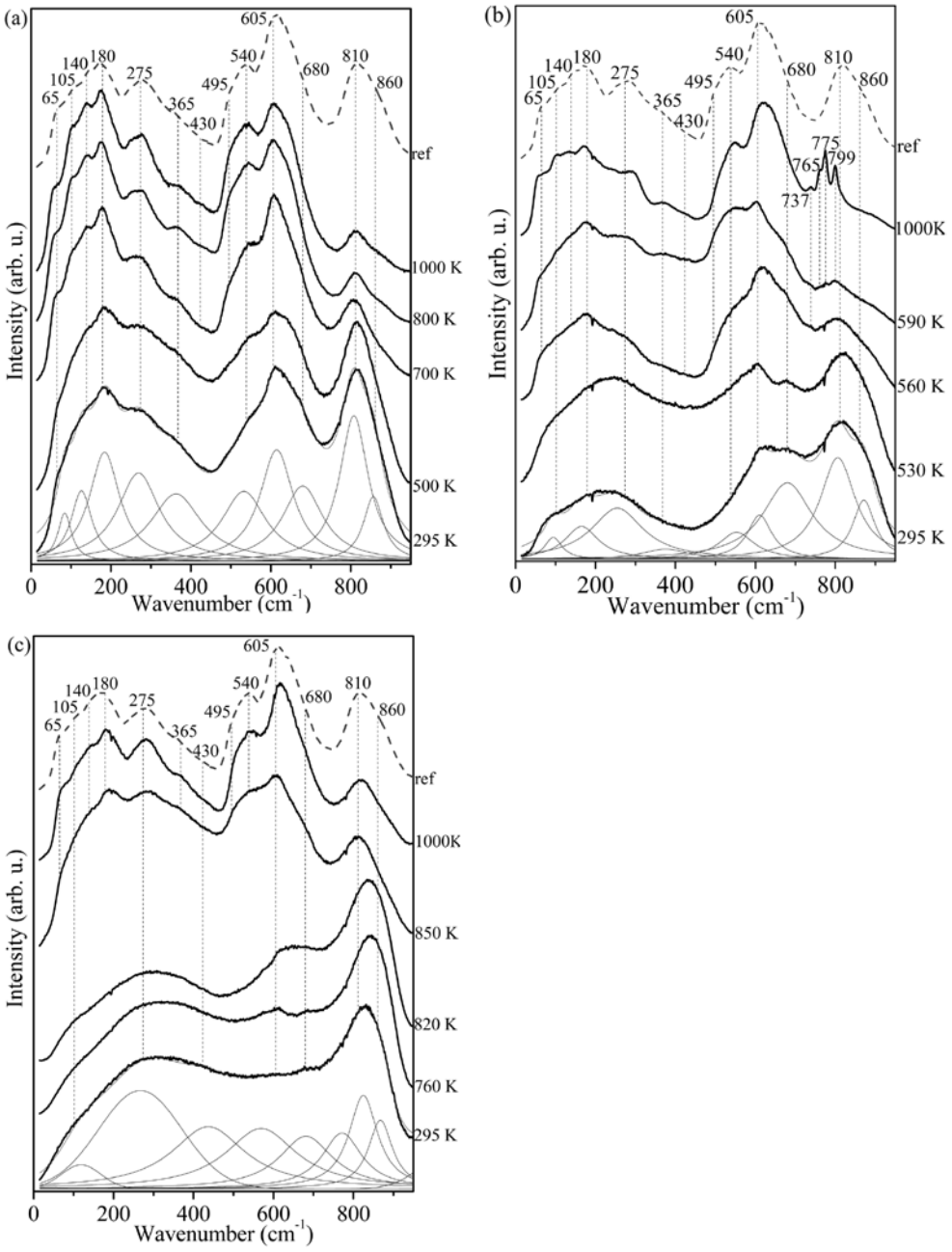


**Fig. 6:** Parallel polarized Raman spectra of weakly damaged (a) Panda Hill, (b) Blue River and (c) Miass pyrochlores at room temperature (ref: reference sample) and after annealing at given temperatures for 1 h individually; the Raman spectrum of non-amorphous Schelingen pyrochlore is shown for comparison.

disappears with the inset of recrystallization at temperatures above 800 K. With increasing crystallinity the 605 $cm^{-1}$ mode ($T_{2g}$) becomes the strongest signal, while the mode near 810 $cm^{-1}$ sharply shrinks.

Vandenborre et al. [58] assumed the 810 $cm^{-1}$ band to be a combination band. A further possible explanation for the appearance of the Raman band near 810 $cm^{-1}$ may be broken selection rules. This would be related to a lower symmetry in the real structure, compared to the ideal arrangement, which would be the case for the relevant short range coordination, if additional vacancies and impurities distort the local symmetry. To verify this assumption, additionally IR spectroscopic measurements have been conducted on the crystalline reference sample from Schelingen. Like the Raman bands, the infrared bands appear strongly broadened, due to impurities and defects. There are two peak intensities centered at 553 and 710 $cm^{-1}$, respectively (Figure 8). Both show right-hand

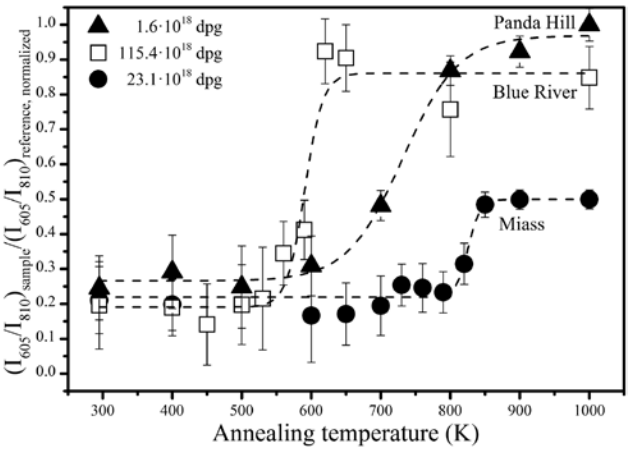


**Fig. 7:** Ratio of the sum of integrated intensities of fitted modes 605 and 680 $cm^{-1}$ divided by the integrated intensity sum of modes 810 and 860 $cm^{-1}$ for weakly amorphous Panda Hill (▲), intermediate Blue River (□) excluding the sharp additional modes and metamict Miass (●) pyrochlores (dashed lines are guide for the eye).

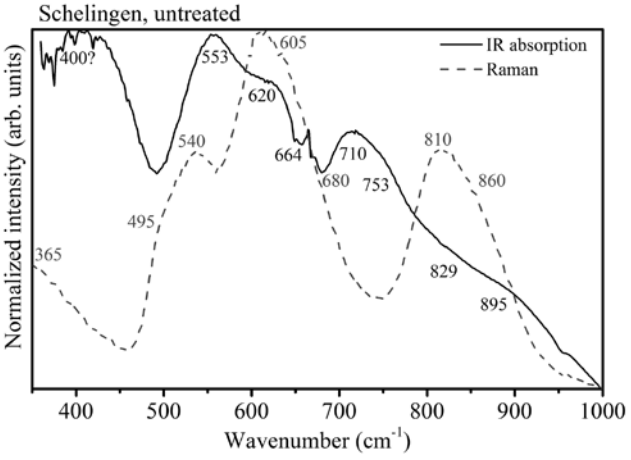


**Fig. 8:** Comparison of Raman and FTIR spectra of the untreated Schelingen sample.

shoulders (centered on 620 and 664 $cm^{-1}$, and 753, 829 and 895 $cm^{-1}$, respectively).

The comparison of Raman and infrared spectra also confirms the violation of the selection rules in pyrochlore. With its centrosymmetric space group simultaneous Raman- and IR-active modes are symmetry forbidden in the pyrochlore structure. Figure 8 shows that the crystalline reference sample has infrared maxima centered at 553, 620, 664 and 829 $cm^{-1}$, corresponding to Raman shifts centered at 540, 605, 680 and 810 $cm^{-1}$. Six of the seven fundamental infrared-active modes were observed between 70 and 523 $cm^{-1}$ in chemically comparable niobate pyrochlores [64, 66]. The seventh mode was assigned to an infrared band between 550 and 850 $cm^{-1}$, which could correspond to the observed band at 553 $cm^{-1}$ in the Schelingen sample. Additional infrared bands within this range are either not fundamental modes or related to clusters with lighter or stronger bond substitutional ions.

## Thermal analysis of the structural reorganization process

The annealing induced thermal behavior of the three investigated radiation-damaged pyrochlore samples from Panda Hill, Blue River and Miass has been additionally studied by combined DSC-TG analysis (Figure 9). The obtained results correlate well with the above mentioned investigations of the annealing related short- and long-range ordering behavior, enable a complete picture of the underlying recrystallization processes.

The weakly damaged Panda Hill sample shows a broad, less defined exothermic DSC signal between ~450 and 800 K, with a maximum around 620 K (Figure 9a). The observed general mass loss during annealing up to ca. 1000 K is around 0.6 %. The temperature range of

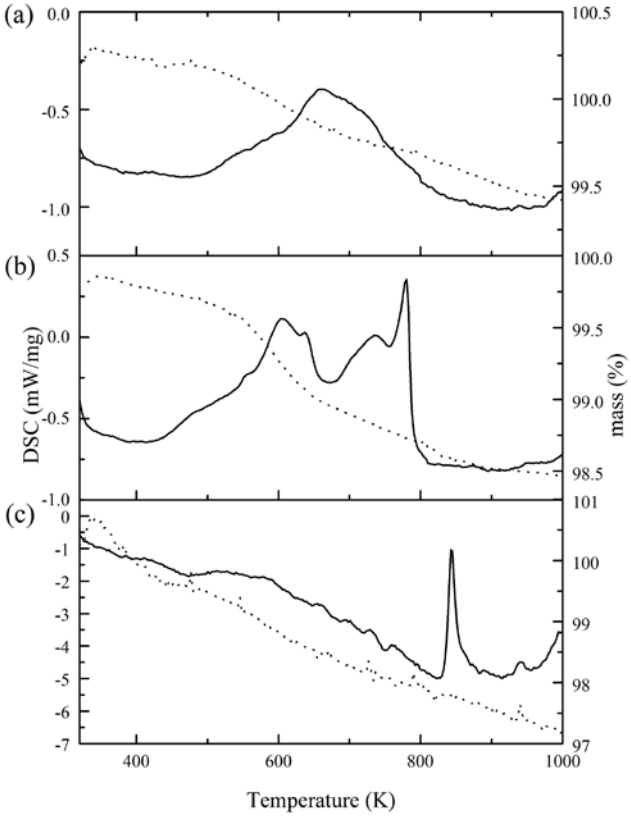


**Fig. 9:** Differential scanning calometry curves (solid line, left axis) and thermogravimetry (dotted line, right axis) of pyrochlores from Panda Hill (a), Blue River (b) and Miass (c).

the observed exothermic reaction, accompanied by an increase in weight loss (Figure 9a), is in very good agreement with the findings of the Raman spectroscopic and powder XRD measurements. This indicates, that the major structural reorganization of this relatively slightly disordered sample takes place between ca. 500 and 800 K (Figures 4, 7, 9a).

The relatively strongly radiation damaged Blue River sample shows in a comparable temperature range to Panda Hill (~435 and 800 K) a broad exothermic DSC feature with at least two prominent maxima. A broader one at ~610 K and a sharp defined one at ~785 K (Figure 9b). The measured mass decrease shows a noticeable increase at temperatures between 560 and 653 K with a general decrease of 1.5 %. Raman spectroscopy revealed an onset of the recrystallization process around 550 K with a strong increase up to ~620 K on the local length scale (Figures 4, 7). This is consistent with DSC results, which show a first broadened exothermic maximum around 610 K (Figure 9b). The Raman measurements indicate further structural ordering up to ca. 800 K, indicated by the second sharp and defined DSC maximum around 785 K (Figures 7, 9b). This ongoing recrystallization is also indicated by the occurrence of the four additional Raman peaks between 730 and 800 $cm^{-1}$ above 560 K (Figures 7, 9b). This observation is consistent with the behavior of the FWHM of the main (440) pyrochlore diffraction signal, which indicates the reestablishment of the long-range order, at least up to ~1000 K (Figure 9b). The main decrease of the amorphous fraction takes place between ca. 650 and 800 K. Hence, the intermediate damaged pyrochlore structure shows first a strong recovery on the local length-scale, followed by the reestablishment of the long range order at slightly higher annealing temperatures.

The DSC curve of the metamict Miass sample (completely amorphous on XRD length scale) shows a strong distinct exothermic peak occurring between 800 and 900 K with a sharp maximum around 840 K (Figure 9c). The observed general mass loss during annealing is around 2.9 % with a distinct drop around 490 K. This range is in good agreement with the results of the Raman spectroscopic and powder XRD measurements which indicate annealing-induced recrystallization between ~800 and 850 K. The observed change of the shape of the Raman signal between 820 and 850 K (Figures 4, 9c) coincides very well with the relatively high enthalpy of the exothermic DSC peak in this temperature region (Figure 9c).

Initially existing crystalline clusters in the radiation damaged pyrochlores (Figure 3) coincide with the observed decrease of the recrystallization temperature (Figures 7, 9). This indicates a reduction of the recrystallization energy in case of existing crystalline seeds. HRTEM studies by Lumpkin et al. [14] revealed in structurally and chemically comparable pyrochlore samples the existence of crystalline "islands" and decreasing crystalline fractions with increasing radiation dose. Similar behavior has been observed e.g. in zircon [90] and titanite [27].

## Conclusion

This study revealed a correlation between the initial structural damage state and the recrystallization of metamict natural pyrochlore. Considerable differences occur during thermally-induced recrystallization depending on the degree of damage. The amorphous fraction was reduced in Panda Hill from 28 % to 14 %, in Blue River from 85 % to 8 % and in Miass from 100 % to 23 % after annealing at T = 1000 K.

The observed differences in the recrystallization lead to a picture of highly recrystallization resistant metamict pyrochlore (Miass) and a significantly less resistant structure with some initial crystalline clusters (Blue River) (Figures 3, 4). Recrystallization of the fully metamict phase takes place in a very narrow temperature window and at the highest annealing temperature of all probed samples. Initially existing crystalline clusters in the Blue River sample result in a stepwise recrystallization process (Figures 4, 9). The weakly radiation-damaged pyrochlore recrystallized rather continuous starting at low annealing temperature. Thermogravimetry showed that the recrystallization is not accompanied by a significant weight loss.

The observed Raman bands of all samples deviate from theoretically predicted modes and are very broad, due to chemical impurities and radiation damage. Nevertheless, the degree of local order could be successfully obtained from the ratio between integrated intensities of prominent spectral features (e.g. Raman bands around 605–680 $cm^{-1}$ and 810–860 $cm^{-1}$ for pyrochlore). According to the longer-ranging X-ray diffraction the thermal recrystallization happens in the temperature interval 500–700 K for Panda Hill, 650–800 K for Blue River and 800–850 K for Miass while the local Raman probe finds recrystallization in ranges 500–800 K for Panda Hill, 550–620 K for Blue River and 820–850 K for Miass, respectively.

High amounts of U and Ta lead to the formation of local modes in the Blue River pyrochlore. This effect occurs above 560 K when the material is still disordered (Figure 3c) and impurity interactions of U/Ta-O stretching modes become prominent (Figure 6b). This has been observed in natural pyrochlore for the first time.

**Acknowledgments:** Financial support by the DFG (SPP 1415) is gratefully acknowledged (P.Z. and U.B.). T.B. is grateful for the support by the DAAD with funds from the BMBF and the People Programme (Marie Curie Actions) of the European Union's Seventh Framework Programme (FP7/2007-2013) under REA grant agreement n° 605728 (P.R.I.M.E. – Postdoctoral position) and also to the University of Hamburg. We would like to thank Stefanie Heidrich for microprobe analysis, Joachim Ludwig for powder XRD measurements and Peter Stutz for sample preparation. The thermal analysis at UC Davis was supported by the U.S. Department of Energy through the Energy Frontier Research Center "Materials Science of Actinides" under Award Number DE-SC001089.

## References

[1] A. Pabst, The metamict state. *Am. Mineral.* **1952**, *37*, 137.
[2] V. Bouska, A systematic review of metamict minerals. *Acta Univ. Carol. Geol.* **1970**, *3*, 143.
[3] R. C. Ewing, The metamict state: 1993 – the centennial. *Nucl. Instrum. Meth. B* **1994**, *91*, 22.
[4] G. R. Lumpkin, T. Geisler-Wierwille, *Minerals and Natural Analogues*, 1st ed., Elsevier Inc, **2012**.
[5] B. P. Mandal, M. Pandey, A. K. Tyagi, $Gd_2Zr_2O_7$ pyrochlore: potential host matrix for some constituents of thoria based reactor's waste. *J. Nucl. Mater.* **2010**, *406*, 238.
[6] G. Sattonnay, S. Moll, L. Thomé, C. Decorse, C. Legros, P. Simon, J. Jagielski, I. Jozwik, I. Monnet, Phase transformations induced by high electronic excitation in ion-irradiated $Gd_2(Zr_xTi_{1-x})_2O_7$ pyrochlores. *J. Appl. Phys.* **2010**, *108*, 103512.
[7] S. Moll, G. Sattonnay, L. Thomé, J. Jagielski, C. Decorse, P. Simon, I. W. J. Monnet Weber, Irradiation damage in $Gd_2Ti_2O_7$ single crystals: Ballistic versus ionization processes. *Phys. Rev.* **2011**, *84*, 64115.
[8] B. C. Chakoumakos, Systematics of the pyrochlore structure type, ideal $A_2B_2X_6Y$. *J. Solid State Chem.* **1984**, *53*, 120.
[9] D. D. Hogarth, C. T. Williams, P. Jones, Primary zoning in pyrochlore group minerals from carbonatites. *Mineral. Mag.* **2000**, *64*, 683.
[10] M. Glerup, O. F. Nielsen, F. W. Poulsen, The structural transformation from the pyrochlore structure, $A_2B_2O_7$, to the fluorite structure, $AO_2$, studied by Raman spectroscopy and defect chemistry modeling. *J. Solid State Chem.* **2001**, *160*, 25.
[11] D. Atencio, R. Gieré, M. B. Andrade, A. G. Christy, P. M. Kartashov, The pyrochlore supergroup of minerals: nomenclature. *Can. Mineral.* **2010**, *48*, 673.
[12] R. C. Ewing, A. Meldrum, L. Wang, S. Wang, Radiation-induced amorphization. *Rev. Mineral. Geochem.* **2000**, *39*, 319.
[13] R. C. Ewing, Actinides and radiation effects: impact on the back-end of the nuclear fuel cycle. *Mineral. Mag.* **2011**, *75*, 2359.
[14] G. R. Lumpkin, R. C. Ewing, Y. Eyal, Preferential leaching and natural annealing of alpha-recoil tracks in metamict betaflte and samarskite. *J. Mater. Res.* **1988**, *3*, 357.
[15] R. C. Ewing, W. J. Weber, J. Lian, Nuclear waste disposal-pyrochlore ($A_2B_2O_7$): Nuclear waste form for the immobilization of plutonium and "minor" actinides. *J. Appl. Phys.* **2004**, *95*, 5949.
[16] G. R. Lumpkin, R. C. Ewing, Alpha-decay damage in minerals of the pyrochlore group. *Phys. Chem. Miner.* **1988**, *16*, 2.
[17] D. D. Hogarth, Classification and nomenclature of the pyrochlore group. *Am. Mineral.* **1977**, *62*, 403.
[18] G. R. Lumpkin, Alpha-decay damage and aqueous durability of actinide host phases in natural systems. *J. Nucl. Mater.* **2001**, *289*, 136.
[19] J. W. Wald, P. Offermann, *Scientific Basis for Nuclear Waste Management V*, (Ed. W. Lutze) Elsevier, New York, p. 369, **1982**.
[20] W. J. Weber, J. W. Wald, Hj. Matzke, Self-radiation damage in actinide host phases of nuclear waste forms. *Mater. Res. Soc. Symp. Proc.* **1985**, *8*, 679.
[21] W. J. Weber, J. W. Wald, Hj. Matzke, *Mater. Lett.* **1985**, *3*, 173.
[22] W. J. Weber, R. C. Ewing, C. R. A. Catlow, T. D. de la Rubia, L. W. Hobbs, C. Kinoshita, H. Matzke, A. T. Motta, M. Nastasi, E. K. H. Salje, E. R. Vance, S. J. Zinkle, Radiation effects in crystalline ceramics for the immobilization of high-level nuclear waste and plutonium. *J. Mat. Res.* **1998**, *13*, 1434.
[23] N. K. Kulkarni, S. Sampath, V. Venugopal, Preparation and characterisation of Pu-pyrochlore: $[La_{1-x}Pu_x]_2Zr_2O_7$ (x = 0–1). *J. Nucl. Mater.* **2000**, *281*, 248.
[24] N. P. Laverov, S. V. Yudintsev, S. V. Stefanovsky, Y. N. Jang, New actinide matrix with pyrochlore structure. *Dokl. Earth Sci.* **2001**, *381*, 1053.
[25] N. P. Laverov, S. V. Yudintsev, T. S. Yudintseva, S. V. Stefanovsky, R. C. Ewing, J. Lian, S. Utsunomiya, L. A. Wang, Effect of radiation on properties of confinement matrices for immobilization of actinide-bearing wastes. *Geol. Ore Deposit.* **2003**, *45*, 423.
[26] B. C. Chakoumakos, R. C. Ewing, Crystal chemical constraints on the formation of actinide pyrochlores. *Mat. Res. Soc. Symp. Proc.* **1985**, *44*, 641.
[27] F. C. Hawthorne, L. A. Groat, M. Raudsepp, N. A. Ball, M. Kimata, F. D. Spike, R. Gaba, N. M. Halden, G. R. Lumpkin, R. C. Ewing, R. B. Greegor, F. W. Lytle, G. R. Ercit, G. R. Rossman, F. J. Wicks, R. A. Ramik, B. L. Sheriff, M. E. Fleet, C. McCammon, Alpha-decay damage in titanite. *Am. Mineral.* **1991**, *76*, 370.
[28] R. C. Ewing, W. J. Weber, F. Clinard, Radiation effects in nuclear waste forms for high-level radioactive waste. *Prog. Nucl. Energ.* **1995**, *29*, 63.
[29] K. O. Trachenko, M. T. Dove, E. K. H. Salje, Atomistic modelling of radiation damage in zircon. *J. Phys. Condens. Matter* **2001**, *13*, 1947.
[30] R. C. Ewing, Displaced by radiation. *Nature* **2007**, *445*, 161.
[31] I. Farnan, H. Cho, W. J. Weber, Quantification of actinide $\alpha$-radiation damage in minerals and ceramics. *Nature* **2007**, *445*, 190.
[32] E. K. H. Salje, R. D. Taylor, D. J. Safarik, J. C. Lashley, L. A. Groat, U. Bismayer, R. J. Evans, R. Friedman, Evidence for direct impact damage in metamict titanite $CaTiSiO_5$. *J. Phys. Condens. Matter* **2012**, *24*, 052202.
[33] W. J. Weber, Models and mechanisms of irradiation-induced amorphization in ceramics. *Nucl. Instrum. Meth. B* **2000**, *166*, 98.
[34] J. Lian, K. B. Helean, B. J. Kennedy, L. M. Wang, A. Navrotsky, R. C. Ewing, The order-disorder transition in ion-irradiated pyrochlore. *Acta Mater.* **2003**, *51*, 1493.

[35] A. A. Digeos, J. A. Valdez, K. E. Sickafus, A. R. Boccaccini, S. Atiq, R. W. Grimes, Glass matrix/pyrochlore phase composites for nuclear wastes encapsulation. *J. Mater. Sci.* **2003**, *38*, 1597.
[36] D. M. Strachan, R. D. Scheele, E. C. Buck, A. E. Kozelisky, R. L. Sell, R. J. Elovich, W. C. Buchmiller, Radiation damage effects in candidate titanates for Pu disposition: zirconolite. *J. Nucl. Mater.* **2005**, *345*, 109.
[37] G. R. Lumpkin, R. C. Ewing, B. C. Chakoumakos, Alpha-recoil damage in zirconolite ($CaZrTi_2O_7$). *J. Mater. Res.* **1986**, *1*, 564.
[38] G. R. Lumpkin, E. M. Foltyn, R. C. Ewing, Thermal recrystallization of alpha-recoil damaged minerals of the pyrochlore structure type. *J. Nucl. Mater.* **1986**, *139*, 113.
[39] M. Jafar, P. Sengupta, S. N. Achary, A. K. Tyagi, Phase evolution and microstructural studies in $CaZrTi_2O_7$(zirconolite)–$Sm_2Ti_2O_7$(pyrochlore) system. *J. Eur. Ceram. Soc.* **2014**, *34*, 4373.
[40] J. Lima-de-Faria, Heat treatment of metamict euxenites, polymignites, yttrotantalites, samarskites, pyrochlores, and allanites. *Min. Mag.* **1958**, *31*, 937.
[41] R. C. Ewing, Environmental impact of the nuclear fuel cycle. In: *Energy, Waste, and the Environment: A Geochemical Perspective* (Eds. R. Giere and P. Stille) Geological Society, London, p. 7, Special Publications, Vol. 236, **2004**.
[42] D. J. Gregg, Y. Zhang, Z. Zhang, I. Karatchevtseva, M. G. Blackford, G. Triani, G. R. Lumpkin, E. R. Vance, Crystal chemistry and structures of uranium-doped gadolinium zirconates. *J. Nucl. Mater.* **2013**, *438*, 144.
[43] N. Tomašić, V. Bermanec, A. Gajović, R. Linari, Metamict minerals: an insight into a relic crystal structure using XRD, Raman spectroscopy, SAED and HRTEM. *Croat. Chem. Acta* **2008**, *81*, 391.
[44] R. C. Ewing, The nuclear fuel cycle: a role for mineralogy and geochemistry. *Elements* **2006**, *2*, 331.
[45] S. Park, M. Lang, C. L. Tracy, J. Zhang, F. Zhang, C. Trautmann, P. Kluth, M. D. Rodriguez, R. C. Ewing, Swift heavy ion irradiation-induced amorphization of $La_2Ti_2O_7$. *Nucl. Instrum. Meth. B* **2014**, *326*, 145.
[46] S. V. Yudintsev, T. S. Livshits, J. Zhang, R. C. Ewing, The behavior of rare-earth pyrochlores and perovskites under ion irradiation. *Dokl. Earth Sci.* **2015**, *461*, 247.
[47] S. S. Shoup, C. E. Bamberger, T. J. Haverlock, J. R. Peterson, Aqueous leachability of lanthanide and plutonium titanates. *J. Nucl. Mater.* **1997**, *240*, 112.
[48] B. D. Begg, N. J. Hess, D. E. McCready, S. Thevuthasan, W. J. Weber, Heavy-ion irradiation effects in $Gd_2(Ti_{2-x}Zr_x)O_7$ pyrochlores. *J. Nucl. Mater.* **2001**, *289*, 188.
[49] B. D. Begg, N. J. Hess, W. J. Weber, R. Devanathan, J. P. Icenhower, S. Thevuthasan, B. P. McGrail, Heavy-ion irradiation effects on structures and acid dissolution of pyrochlores. *J. Nucl. Mater.* **2001**, *288*, 208.
[50] Y. Zhang, K. P. Hart, W. L. Bourcier, R. A. Day, M. Colella, B. Thomas, Z. Aly, A. Jostsons, Kinetics of uranium release from Synroc phases. *J. Nucl. Mater.* **2001**, *289*, 254.
[51] J. P. Icenhower, E. A. Rodriguez, D. M. Strachan, J. L. Steele, M. M. Lindberg, *Dissolution Kinetics of Titanate-Based Ceramic Waste Forms: Results from Single-Pass Flow Tests on Radiation Damaged Specimens*, Pacific Northwest National Laboratory, Richland, **2003**.
[52] T. Geisler, J. Berndt, H. W. Meyer, K. Pollok, A. Putnis, Low-temperature aqueous alteration of crystalline pyrochlore: correspondence between nature and experiment. *Mineral. Mag.* **2004**, *68*, 905.
[53] G. R. Lumpkin, K. L. Smith, R. Giere, C. T. Williams, *Geochemical Behaviour of Host Phases for Actinides and Fission Products in Crystalline Ceramic Nuclear Waste Forms*. Geological Society, Special Publications, London, Vol. 236, **2004**, p. 89.
[54] M. Lang, F. Zhang, J. Zhang, J. Wang, J. Lian, W. J. Weber, B. Schuster, C. Trautmann, R. Neumann, R. C. Ewing, Review of A2B2O7 pyrochlore response to irradiation and pressure. *Nucl. Instr. Meth. Phys. Res. B* **2010**, *268*, 2951.
[55] K. B. Helean, A. Navrotzky, G. R. Lumpkin, M. Collela, J. Lian, R. C. Ewing, B. Ebbinghaus, J. G. Catalano, Enthalpies of formation of U-, Th-, Ce-brannerite: implications for plutonium immobilization. *J. Nucl. Mater.* **2003**, *320*, 231.
[56] K. B. Helean, S. V. Ushakov, C. E. Brown, A. Navrotsky, J. Lian, R. C. Ewing, J. M. Farmer, L. A. Boatner, Formation enthalpies of rare earth titanate pyrochlore. *J. Solid State Chem.* **2004**, *177*, 1858.
[57] Y. Li, X. Zhu, T. A. Kassab, Atomic-scale microstructures, Raman spectra and dielectric properties of cubic pyrochlore-typed $Bi_{1.5}MgNb_{1.5}O_7$ dielectric ceramics. *Ceram. Int.* **2014**, *40*, 8125.
[58] M. T. Vandenborre, E. Husson, J. P. Chatry, D. Michel, Rare-earth titanates and stannates of pyrochlore structure; vibrational spectra and force fields. *J. Raman Spectrosc.* **1983**, *14*, 63.
[59] B. Mihailova, S. Stoyanov, V. Gaydarov, M. Gospodinov, L. Konstantinov, Raman spectroscopy study of pyrochlore $Pb_2Sc_{0.5}Ta_{l.5}O_{6.5}$ crystals. *Solid State Commun.* **1997**, *103*, 623.
[60] S. Kamba, V. Porokhonskyy, A. Pashkin, V. Bovtun, J. Petzelt, J. Nino, S. Trolier-McKinstry, M. Lanagan, C. Randall, Anomalous broad dielectric relaxation in $Bi_{1.5}Zn_{1.0}Nb_{1.5}O_7$ pyrochlore. *Phys. Rev. B* **2002**, *66*, 1.
[61] C. M. Ronconi, O. L. Alves, Structural evolution and optical properties of $Cd_2Nb_2O_7$ films prepared by metallo-organic decomposition. *Thin Solid Films* **2003**, *441*, 121.
[62] W. Hong, D. Huiling, Y. Xi, Structural study of $Bi_2O_3$-ZnO-$Nb_2O_5$ based pyrochlores. *Mat. Sci. Eng. B* **2003**, *99*, 20.
[63] Q. Wang, H. Wang, X. Yao, Structure, dielectric and optical properties of $Bi_{1.5}ZnNb_{1.5-x}Ta_xO_7$ cubic pyrochlores. *J. Appl. Phys.* **2007**, *101*, 104116.
[64] M. Fischer, T. Malcherek, U. Bismayer, P. Blaha, K. Schwarz, Structure and stability of $Cd_2Nb_2O_7$ and $Cd_2Ta_2O_7$ explored by ab initio calculations. *Phys. Rev. B* **2008**, *78*, 14108.
[65] T. T. A. Lummen, I. P. Handayani, M. C. Donker, D. Fausti, G. Dhalenne, P. Berthet, A. Revcolevschi, P. H. M. Van Loosdrecht, Phonon and crystal field excitations in geometrically frustrated rare earth titanates. *Phys. Rev. B* **2008**, *77*, 1.
[66] D. J. Arenas, L. V. Gasparov, W. Qiu, J. C. Nino, C. H. Patterson, D. B. Tanner, Raman study of phonon modes in bismuth pyrochlores. *Phys. Rev. B* **2010**, *82*, 1.
[67] A. N. Radhakrishnan, P. P. Rao, K. S. M. Linsa, M. Deepa, P. Koshy, Influence of disorder-to-order transition on lattice thermal expansion and oxide ion conductivity in $(Ca_xGd_{1-x})_2(Zr_{1-x}M_x)_2O_7$ pyrochlore solid solutions. *Dalton Trans.* **2011**, *40*, 3839.
[68] D. S. D. Gunn, N. L. Allan, H. Foxhall, J. H. Harding, J. A. Purton, W. Smith, M. J. Stein, I. T. Todorov, K. P. Travis, Novel potentials for modelling defect formation and oxygen vacancy migration in $Gd_2Ti_2O_7$ and $Gd_2Zr_2O_7$ pyrochlores. *J. Mater. Chem.* **2012**, *22*, 4675.
[69] V. S. Urusov, A. E. Grechanovsky, N. N. Eremin, Molecular dynamics study of self-radiation damage in $Gd_2Zr_2O_7$ and $Gd_2Ti_2O_7$ pyrochlores. *Dokl. Phys.* **2014**, *59*, 263.

[70] A. Archer, H. R. Foxhall, N. L. Allan, D. S. D. Gunn, J. H. Harding, I. T. Todorov, K. P. Travis, J. A. Purton, Order parameter and connectivity topology analysis of crystalline ceramics for nuclear waste immobilization. *J. Phys. Condens. Matter* **2014**, *26*, 485011.

[71] P. K. Kulriya, R. Kumari, R. Kumar, V. Grover, R. Shukla, A. K. Tyagi, D. K. Avasthi, In-situ high temperature irradiation setup for temperature dependent structural studies of materials under swift heavy ion irradiation. *Nucl. Instrum. Meth. B* **2015**, *342*, 98.

[72] H. Lippolt, J. W. Gentner, W. Wimmenauer, Altersbestimmungen nach der Kalium-Argon-Methode an tertiären Eruptivgesteinen Südwestdeutschlands. *Jahreshefte des Geologischen Landesamtes Baden-Württemberg* **1963**, *6*, 507.

[73] K. Bell, J. Blenkinsop, Nd and Sr isotopic compositions of East African carbonatites: implications for mantle heterogeneity. *Geology* **1987**, *15*, 99.

[74] V. Berger, D. Singer, G. Orris, Carbonatites of the world, explored deposits of Nb and REE – database and grade and tonnage models. US Geological Survey, Reston, Virginia, **2009**, 1.

[75] A. A. Krasnobaev, A. I. Rusin, P. M. Valizer, S. V. Busharina, Zirconology of calcite carbonatite of the Vishnevogorsk massif, southern Urals. *Dok. Earth Sci.* **2010**, *431*, 390.

[76] H. Holland, D. Gottfried, The effect of nuclear radiation on the structure of zircon. *Acta Crystallogr.* **1955**, *8*, 291.

[77] M. E. Wieser, N. Holden, T. B. Coplen, J. K. Böhlke, M. Berglund, W. A. Brand, P. De Bièvre, M. Gröning, R. D. Loss, J. Meija, T. Hirata, T. Prohaska, R. Schoenberg, G. O'Connor, T. Walczyk, S. Yoneda, X.-K. Zhu, Atomic weights of the elements 2001 (IUPAC Technical Report). *Pure Appl. Chem.* **2013**, *85*, 1047.

[78] E. Kroumova, M. I. Aroyo, J. M. Perez-Mato, A. Kirov, C. Capillas, S. Ivantchev, H. Wondratschek, Bilbao crystallographic server: useful databases and tools for phase-transition studies. *Phase Transit.* **2003**, *76*, 155.

[79] J. Zhang, J. Lian, F. Zhang, J. Wang, A. F. Fuentes, R. C. Ewing, Intrinsic structural disorder and radiation response of nanocrystalline $Gd_2(Ti_{0.65}Zr_{0.35})_2O_7$ Pyrochlore. *J. Phys. Chem. C* **2010**, *114*, 11810.

[80] M. Mączka, J. Hanuza, K. Hermanowicz, A. F. Fuentes, K. Matsuhira, Z. Hiroi, Temperature-dependent Raman scattering studies of the geometrically frustrated pyrochlores $Dy_2Ti_2O_7$, $Gd_2Ti_2O_7$ and $Er_2Ti_2O_7$. *J. Raman Spectrosc.* **2008**, *39*, 5537.

[81] S. Saha, S. Prusty, S. Singh, R. Suryanarayanan, A. Revcolevschi, A. K. Sood, Anomalous temperature dependence of phonons and photoluminescence bands in pyrochlore $Er_2Ti_2O_7$: signatures of structural deformation at 130 K Surajit. *J. Phys. Condens. Matter* **2011**, *23*, 445402.

[82] M. Mączka, M. Sanjuán, A. Fuentes, L. Macalik, J. Hanuza, K. Matsuhira, Z. Hiroi, Temperature-dependent studies of the geometrically frustrated pyrochlores $Ho_2Ti_2O_7$ and $Dy_2Ti_2O_7$. *Phys. Rev. B* **2009**, *79*, 1.

[83] M. Lang, J. Lian, J. Zhang, F. Zhang, W. J. Weber, C. Trautmann, R. C. Ewing, Single-ion tracks in $Gd_2Zr_{2-x}Ti_xO_7$ pyrochlores irradiated with swift heavy ions. *Phys. Rev. B* **2009**, *79*, 1.

[84] G. Sattonnay, N. Sellami, L. Thomé, C. Legros, C. Grygiel, I. Monnet, J. Jagielski, I. Jozwik-Biala, P. Simon, Structural stability of $Nd_2Zr_2O_7$ pyrochlore ion-irradiated in a broad energy range. *Acta Mater.* **2013**, *61*, 6492.

[85] N. J. Hess, B. D. Begg, S. D. Conradson, D. E. McCready, P. L. Gassman, W. J. Weber, Spectroscopic investigations of the structural phase transition in $Gd_2(Ti_{1-y}Zr_y)_2O_7$ pyrochlores. *J. Phys. Chem. B* **2002**, *106*, 4663.

[86] B. P. Mandal, N. Garg, S. M. Sharma, A. K. Tyagi, Solubility of $ThO_2$ in $Gd_2Zr_2O_7$: XRD, SEM and Raman spectroscopic studies. *J. Nucl. Mater.* **2009**, *392*, 95.

[87] R. L. Frost, S. J. Palmer, Reddy B. J., Raman spectroscopic study of the uranyl titanite mineral euxenite (Y, Ca, U, Ce, Th)(Nb, Ta, Ti)$_2O_6$. *J. Raman Spectrosc.* **2011**, *42*, 1160.

[88] L. Francis, P. P. Rao, M. Thomas, S. K. Mahesh, V. R. Reshmi, T. S. Sreene, Structural influence on the photoluminescence properties of $Eu^{3+}$ doped $Gd_3MO_7$ (M = Nb, Sb, and Ta) red phosphors. *Phys. Chem. Chem. Phys.* **2014**, *16*, 17108.

[89] I. F. Chang, S. S. Mitra, Long wavelength optical phonons in mixed crystals. *Adv. Phys.* **1971**, *20*, 359.

[90] T. Murakami, B. C. Chakoumakos, R. C. Ewing, G. R. Lumpkin, W. J. Weber, Alpha-decay event damage in zircon. *Am. Mineral.* **1991**, *76*, 1510.